

Phase-field simulation dendritic growth under forced convection with hypergravity

Jianjing Zheng(郑建靖), Xuanxuan Zhou(周旋旋), Daosheng Ling(凌道盛), and Kunming Song(宋坤明)
Citation: Chin. Phys. B, 2025, 34 (**10**): 108102. DOI: 10.1088/1674-1056/ade068
http://cpb.iphy.ac.cn; http://iopscience.iop.org/cpb

What follows is a list of articles you may be interested in

Exploration of the coupled lattice Boltzmann model based on a multiphase field model: A study of the solid-liquid-gas interaction mechanism in the solidification process

Chang-Sheng Zhu(朱昶胜), Li-Jun Wang(王利军), Zi-Hao Gao(高梓豪), Shuo Liu(刘硕), and Guang-Zhao Li(李广召)
Chin. Phys. B, 2024, 33 (**3**): 038101. DOI: 10.1088/1674-1056/ad1a91

Parameter calculation and result storage for phase-field simulation in α-Mg dendrite growth of Mg-5-wt% Zn alloy

Wei-Peng Chen(陈伟鹏), Hua Hou(侯华), Yun-Tao Zhang(张云涛), Wei Liu(柳伟), and Yu-Hong Zhao(赵宇宏)
Chin. Phys. B, 2023, 32 (**11**): 118103. DOI: 10.1088/1674-1056/acd7e3

GPU parallel computation of dendrite growth competition in forced convection using the multi-phase-field-lattice Boltzmann model

Zi-Hao Gao(高梓豪), Chang-Sheng Zhu(朱昶胜), and Cang-Long Wang(王苍龙)
Chin. Phys. B, 2023, 32 (**7**): 078101. DOI: 10.1088/1674-1056/acbc68

A lattice Boltzmann-cellular automaton study on dendrite growth with melt convection in solidification of ternary alloys

Dong-Ke Sun(孙东科), Zhen-Hua Chai(柴振华), Qian Li(李谦), Guang Lin(林光)
Chin. Phys. B, 2018, 27 (**8**): 088105. DOI: 10.1088/1674-1056/27/8/088105

Effects of physical parameters on the cell-to-dendrite transition in directional solidification

Wei Lei (魏雷), Lin Xin (林鑫), Wang Meng (王猛), Huang Wei-Dong (黄卫东)
Chin. Phys. B, 2015, 24 (**7**): 078108. DOI: 10.1088/1674-1056/24/7/078108

Phase-field simulation dendritic growth under forced convection with hypergravity

Jianjing Zheng(郑建靖)[1,2,†], Xuanxuan Zhou(周旋旋)[1,2], Daosheng Ling(凌道盛)[1,2], and Kunming Song(宋坤明)[1,2]

[1] *Institute of Hypergravity Science and Technology, Zhejiang University, Hangzhou* 310058, *China*

[2] *Key Laboratory of Soft Soils and Geoenvironmental Engineering (Ministry of Education), Zhejiang University, Hangzhou* 310058, *China*

(Received 16 March 2025; revised manuscript received 10 May 2025; accepted manuscript online 4 June 2025)

The phase-field method is used to study the free dendritic crystal growth under forced convection with hypergravity, the hypergravity term is introduced into the liquid-phase momentum equation to examine the dendritic growth. The paper focuses on the morphology of dendrite growth as well as the tip radius of the upstream dendritic arm and the average growth velocity of dendrite tips under different hypergravity levels. The results show that the morphology of dendrite changes significantly under represent simulation conditions when the hypergravity reaches $35\boldsymbol{g}_0$, the upstream dendritic arm will bifurcate and the horizontal dendrite arms gradually tilt upwards. This change is mainly caused by the hypergravity and flow changing the temperature field near the dendrite interface. In addition, before the morphology of the dendrite is significantly altered, the radius of the tip of the dendrite upstream arm becomes larger with the increase in hypergravity, and the average growth velocity will increase linearly with it. The morphology of dendritic growth under different hypergravity and the changes in the tip radius along with the average growth velocity of the upstream dendritic tip with hypergravity are given in this paper. Finally, the reasons for these phenomena are analyzed.

Keywords: hypergravity, dendrite growth, phase-field simulation, forced convection

PACS: 81.10.Aj

DOI: 10.1088/1674-1056/ade068 **CSTR:** 32038.14.CPB.ade068

1. Introduction

The convection phenomenon inevitably exists in the solidification process of metallic material melts. In fact, convection is present in almost all solidified dendritic growth experiments of metal melts on the ground. The problem of dendrite growth under flow has been a popular research theme for a long time, and many results have been achieved by the academic community in the study of the effect of flow on dendritic growth. Phase-field modeling of coupled flow was first developed by Beckermann *et al.*[1] They explored the free dendrite growth under flow and systematically studied the dendrite growth velocity, dendrite tip radius and selection parameters under flow. Tong *et al.*[2] performed similar simulations and introduced the effect of noise in the energy equation in the phase-field model to study the impact of flow on the growth of secondary dendrite arms. The results show that the flow causes asymmetric growth of dendrites, and it has a promoting effect on the growth of the upstream dendrite arms, has almost no impact on the growth of the dendrite arms normal to flow, and has an inhibiting effect on the growth of the downstream dendrite arm. Subsequently, the phase-field method has been widely used to simulate the 2D dendritic growth in alloys. Zhang *et al.*[3] studied the pattern selection in crystal growth under melt flows using the anisotropic lattice Boltzmann phase-field method. The results demonstrate that melt flows can affect the growth process and change the final crystal morphology. The melt flow promotes the growth of crystal upstream arms while it retards the growth of downstream arms. The interface normal angle distribution reflects symmetrical and asymmetrical features of crystal morphologies, and the interface curvature distribution reflects the complexity and variation of growth velocities. Zhu *et al.*[4] simulated the competitive crystal growth of binary alloy for directional solidification using the multiphase field method. The results show that the thermal gradient has a great influence on the growth of dendrites. In the low thermal gradient state, the number of dendrites within the interface is fewer, the morphological levels of the dendrites at the two different angles are more distinct, and the dendrites have a strong branching capability. However, in the high thermal gradient state, the number of dendrites in the interface gradually increases and the branching capability of two different angles of dendrites decreases.

In recent decades, numerical simulations of 3D dendritic growth under melt flow have been widely conducted. Lu[5] and Jeong *et al.*[6] simulated the growth of pure-substance dendrites under 3D flow conditions using the phase-field method. It was found that in the 3D simulation, the side branching induced by the flow appears along the upstream arm, and some at the upstream side of the horizontal dendrite arms when the flow velocity is significantly large with low undercooling. Recently, Chen *et al.*[7] and Gong *et al.*[8] conducted 2D simulation of dendritic growth and found that the flow will cause

†Corresponding author. E-mail: zhengjianjing@zju.edu.cn

© 2025 Chinese Physical Society and IOP Publishing Ltd. All rights, including for text and data mining, AI training, and similar technologies, are reserved.

a large temperature difference near the tips of the upstream dendrite arms. This temperature difference will result in a significant difference in the morphology of the dendrite, and the horizontal dendrite arms will tilt under the high flow velocity. Qiu *et al.*[9] studied the fully coupled thermal-solute-convection dendrite growth of Al–Cu alloy. Their study shows that dendrite tilting and tip splitting may be attributed to the strong convection effect in the melt, which weakens the inherent anisotropy during dendrite growth. By dendrite tilting and tip splitting, the dendrite growth tries to adapt to the local thermodynamic conditions.

Different forms of solidification correspond to different types of dendritic growth, and these microstructures significantly affect the physical and mechanical properties of the materials.[10] Therefore, during the solidification process, additional physical fields are used, such as hypergravity fields, which are often applied to improve the microstructure of materials during solidification to obtain materials with good properties.[11,12] In recent years, it has been shown that hypergravity has a significant effect on the microstructure dendritic growth during the solidification process of materials.[13–15] The problem of dendritic growth under forced convection with hypergravity has attracted extensive attention in the academic community. Li *et al.*[16] and Jin *et al.*[17] conducted experiments on the growth of dendrites and cellular crystals under normal gravity flow. The results show that the gravity-induced flow causes downstream deflection of dendrites and cellular crystals, while gravity-induced flow causes bifurcation of the tip of the cellular crystals. Zimmermann *et al.*[18] conducted experiments on the growth of NPG-37.5 wt% DC alloy dendrites under hypergravity. The results show that the quantity of nucleation of equiaxed dendrites increases significantly with increasing hypergravity, and the settling rate is also accelerated significantly. At the same hypergravity level, increasing the cooling rate will accelerate the growth velocity of the dendrite tip.

Due to the high cost and the difficulty in observing changes in physical quantities during the solidification process under hypergravity conditions, hypergravity experiments are rarely conducted. Numerical simulation, as an efficient technical method, can effectively restore various fields, such as temperature and velocity fields, during the solidification process. This capability allows one to have a deeper understanding of the microscopic mechanisms involved in solidification and it has been widely used. Zhang *et al.*[19] used the phase-field method to simulate steady-state free dendrite growth under hypergravity conditions by coupling the hypergravity into the heat transfer coefficient. They explored the growth morphology of dendrites under different hypergravity and found that the hypergravity caused the dendrites to show asymmetric growth. Along the direction of the hypergravity, the growth rate of the dendrites accelerated, perpendicular to the direction of the hypergravity growth, the growth rate slowed down, and the dendrites produced numerous secondary dendrites that grew along the direction of the hypergravity. Steinbach[20] simulated the vertically oriented dendrite growth of Al–Cu alloys under horizontal flow with the vertical hypergravity, and found that the hypergravity induces convection loops. When the loops are opposite to the direction of the dendrite growth, it promotes the dendrite growth, and the convection loops induced by the hypergravity affect the horizontal spacing of the stabilized growth between the dendrites. Viardin *et al.*[21] performed numerical simulations of dendrite growth of Ti–Al alloys under different flow conditions with hypergravity. The results show that hypergravity inhibits the growth of Ti columnar dendrites when the hypergravity is in the opposite direction to the dendritic growth. Furthermore, the dendrites will split during their growth when the hypergravity reaches a certain level. However, when the hypergravity is in the same direction as the dendrite growth, the hypergravity can promote the growth. In addition, the hypergravity will affect the spacing of the secondary dendrite arms. Zhang *et al.*[22] investigated the effect of hypergravity on the dendritic growth characteristics of aluminum alloy using the numerical simulation. It shows that the hypergravity changed the symmetry of the solute distribution and the morphology of dendrites. With increasing hypergravity, the asymmetry of dendrites increased. In addition, hypergravity greatly increased the flow rate of the solute-rich liquid phase between dendrites, resulting in channel segregation.

These experiments successfully explored the impact of forced convection under hypergravity on dendrite growth. However, the experimental phenomena have not yet been understood from a mechanistic perspective. The numerical simulations successfully explained the experimental phenomena in certain aspects and simulated the growth of dendrites under the effect of hypergravity, but they did not rigorously derive a phase-field model for coupled hypergravity under convection in detail. Furthermore, they did not explain the effect of hypergravity on the dendritic interface specifically to further investigate the impact of hypergravity and flow pattern on dendrite growth.

In this paper, the phase-field model of coupled hypergravity is rigorously derived, and the forced flow free dendrite growth under hypergravity is simulated to investigate the effect of hypergravity on the dendrite growth. The morphologies of dendritic growth under different hypergravity are given in the paper, and the reasons for some typical morphologies are explained. It is found that the morphology of dendrite changes significantly when the hypergravity reaches a certain level, and the upstream dendritic arm will bifurcate and the horizontal arms will gradually tilt upwards. These phenomena are consistent with the equiaxed dendrite growth observed

under hypergravity[18] and columnar dendritic growth under hypergravity convection,[23] as shown in Fig. 1. Finally, the hypergravity will affect the tip radius and average growth rate of the upstream dendritic arm.

The structure of this paper is as follows. The introduction is first, followed by Section 2, which discusses how to introduce the hypergravity term in the momentum equation, respectively. Section 3 mainly shows the numerical method, computational domain, mesh, and initial and boundary conditions used in the simulation. Section 4 focuses on the current simulation results, mainly including the reliability verification of the numerical simulation results, the growth morphologies of dendrites under different hypergravity effects, the effects of hypergravity on the tip radius of the upstream dendrite arm and the average growth rate. Section 5 provides the main conclusions and some future prospects.

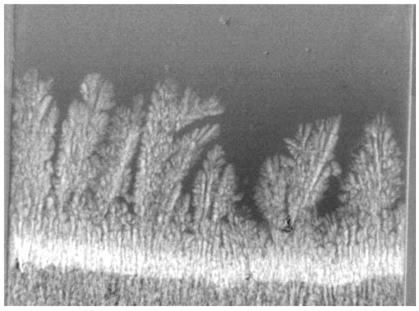


Fig. 1. Experimental results of Abou-Khalil *et al.*[23] Dendritic arm bifurcate growth under hypergravity.

2. Phase-field modeling of dendrite growth coupled with hypergravity

The phase-field model used in this study is mainly based on the pure matter dendrite growth model under flow proposed by Karma *et al.*[24,25] and Tong *et al.*[2] based on phenomenology, which couples the melt flow and temperature field and is a commonly used model to simulate the pure substance dendrite growth under the melt flow. Based on this model, this paper investigates the effect of hypergravity on dendrite growth by introducing a hypergravity term in the momentum equation.

The anisotropic phase-field equation established based on the free energy can be expressed as

$$\begin{aligned}\boldsymbol{\tau}(\boldsymbol{n})\frac{\partial\phi}{\partial t} &= \nabla\cdot\left[\boldsymbol{W}(\boldsymbol{n})^2\nabla\phi\right]+\partial_x\left[|\nabla\phi|^2\boldsymbol{W}(\boldsymbol{n})\frac{\partial\boldsymbol{W}(\boldsymbol{n})}{\partial(\partial_x\phi)}\right]\\ &\quad+\partial_y\left[|\nabla\phi|^2\boldsymbol{W}(\boldsymbol{n})\frac{\partial\boldsymbol{W}(\boldsymbol{n})}{\partial(\partial_y\phi)}\right]\\ &\quad+\phi-\phi^3-\lambda u\left(1-\phi^2\right)^2,\end{aligned}\tag{1}$$

where ϕ denotes the phase-field variable, $\phi=1$ for the solid phase and $\phi=-1$ for the liquid phase. When ϕ is in the range of -1 to 1, this indicates the interfacial region between the solid phase and the liquid phase. ϕ varies continuously and smoothly between -1 and 1 as a function of time and space. $\boldsymbol{W}(\boldsymbol{n})$ denotes the thickness of the diffusion interface with respect to the interfacial normal direction, $\boldsymbol{W}(\boldsymbol{n})=W_0\boldsymbol{a_s}(\boldsymbol{n})$, $\boldsymbol{a_s}(\boldsymbol{n})=1+\varepsilon\cos(4\theta)$, $\boldsymbol{\tau}(\boldsymbol{n})$ is the relaxation time, $\boldsymbol{\tau}(\boldsymbol{n})=\tau_0\left[\boldsymbol{a_s}(\boldsymbol{n})\right]^2$ and λ denotes the coupling coefficient of the phase field and the temperature field.

The energy equation coupled with the phase-field variables can be expressed as

$$\frac{\partial u}{\partial t}+\frac{1}{2}(1-\phi)\boldsymbol{V}\cdot\boldsymbol{V}u=D\boldsymbol{V}^2u+\frac{1}{2}\frac{\partial\phi}{\partial t},\tag{2}$$

where u denotes the dimensionless temperature, $u=\frac{T-T_\mathrm{m}}{L/C_\mathrm{p}}$, T_m is the melt equilibrium temperature, L and C_p denote latent heat and specific heat capacity, respectively, D is the thermal diffusion coefficient, and $\boldsymbol{V}$ denotes the melt flow velocity.

The continuity equation coupled with the phase-field variables can be expressed as

$$\nabla\cdot\left[\frac{1}{2}(1-\phi)\rho\boldsymbol{V}\right]=0.\tag{3}$$

The momentum equation introducing the hypergravity term can be obtained from the convective diffusion equation in a general form. The convective diffusion equation at a point,

$$\frac{\partial(\rho\varphi)}{\partial t}+\nabla\cdot(\rho\boldsymbol{v}\varphi)+\nabla\cdot\boldsymbol{J}=0,\tag{4}$$

where ρ indicates the density, $\boldsymbol{v}$ indicates the velocity of diffusion, $\boldsymbol{J}$ indicates the diffusion flux, and φ denotes any conserved quantity.

For any phase k, integrate over the control body:

$$\begin{aligned}&\frac{\partial\langle X_k\rho\varphi\rangle}{\partial t}+\nabla\cdot\langle X_k\rho\boldsymbol{v}\varphi\rangle+\nabla\cdot\langle X_k\boldsymbol{J}\rangle\\ &-\langle[\rho\varphi(\boldsymbol{v}-\boldsymbol{v}_i)+\boldsymbol{J}]^k\cdot\nabla X_k\rangle=0,\end{aligned}\tag{5}$$

where $\boldsymbol{v}_i$ is the velocity of interfacial motion, X_k is the phase rate of a microscopic arbitrary k phase, and the phase-field variable can be expressed as the microscopic solid-phase ratio $\phi=\phi_s=1-\phi_l=\frac{1}{\Delta V}\int X_s\,\mathrm{d}V=\langle X_s\rangle$, $\langle X_s\rangle$ expresses the average volume of X_s, ϕ_s indicates the solid-phase ratio and ϕ_l indicates the liquid-phase ratio.

Now, there is conserved quantity $\varphi=\boldsymbol{V}$ and source term $\boldsymbol{J}=-\boldsymbol{G}+\boldsymbol{P}-\boldsymbol{\tau}$, where $\boldsymbol{G}=\begin{pmatrix}x\rho g_x\\ y\rho g_y\\ z\rho g_z\end{pmatrix}$ is the gravitational potential function (GPF), $\boldsymbol{P}_l=\begin{pmatrix}p_x\\ p_y\\ p_z\end{pmatrix}$ is the pressure and $\boldsymbol{\tau}=\begin{pmatrix}\tau_x\\ \tau_y\\ \tau_z\end{pmatrix}$ is the shear stress. Substituting them into the equation gives

$$\begin{aligned}&\frac{\partial}{\partial t}\left[(1-\phi)\rho\boldsymbol{V}\right]+\nabla\cdot\left[(1-\phi)\rho\boldsymbol{V}\boldsymbol{V}\right]\\ &=\nabla\left[(1-\phi)\boldsymbol{G}\right]-\nabla\left[(1-\phi)\boldsymbol{P}_l\right]+\nabla\cdot\left[(1-\phi)\boldsymbol{\tau}_l\right]\\ &\quad+\langle[\rho\boldsymbol{V}(\boldsymbol{v}-\boldsymbol{v}_i)-\boldsymbol{G}+\boldsymbol{P}-\boldsymbol{\tau}]^l\cdot\nabla x_l\rangle.\end{aligned}\tag{6}$$

We use the same assumptions as Beckermann *et al.*[1]

(1) The flow velocity of the solid phase is zero, i.e., the flow velocity of the liquid phase is the relative flow velocity based on the solid phase.

(2) The liquid phase is incompressible and in microscopic pressure equilibrium.

(3) The liquid-phase flow velocity $\boldsymbol{V}$ decays linearly to zero from the liquid phase to the solid phase.

For the equations in $\nabla\cdot[(1-\phi)\boldsymbol{\tau}_l]$, assuming that the fluid is incompressible and Newtonian, and the kinematic viscosity of fluid μ_l is constant, there would be $\nabla\cdot[(1-\phi)\boldsymbol{\tau}_l] = \nabla\cdot(\mu_l\nabla[(1-\phi)\boldsymbol{V}])$.

The last term in the above equation is now analyzed one by one.

For $\langle[\boldsymbol{P}]^l\cdot\nabla X_l\rangle$, the above assumption (2) is applied, there would be $\langle[\boldsymbol{P}]^l\cdot\nabla X_l\rangle = \boldsymbol{P}_l\cdot\nabla\phi_l = \boldsymbol{P}_l\cdot\nabla(1-\phi)$, combined with $\nabla[(1-\phi)\boldsymbol{P}_l]$, and the pressure term will be $(1-\phi)\nabla\boldsymbol{P}_l$.

For $\langle[\boldsymbol{\tau}]^l\cdot\nabla X_l\rangle$, there is $\langle[\boldsymbol{\tau}]^l\cdot\nabla X_l\rangle = \boldsymbol{\tau}_l\cdot\nabla\phi_l = \boldsymbol{\tau}_l\cdot\nabla(1-\phi) = \boldsymbol{M}_l^d$, Since the viscous stress is generally proportional to the fluid kinematic viscosity and velocity gradient, adopting assumption (3), analogous to the force of the dissipation term for porous media flow, using the first-order approximation, we have $\boldsymbol{M}_l^d = h\mu_l\phi\frac{\boldsymbol{V}}{W_0}|\nabla\phi|$.

For $\langle[\boldsymbol{G}]^l\cdot\nabla X_l\rangle$, similarly, there is $\langle[\boldsymbol{G}]^l\cdot\nabla X_l\rangle = \boldsymbol{G}\cdot\nabla(1-\phi)$, combining and simplifying with $\nabla[(1-\phi)\boldsymbol{G}]$, $\nabla[(1-\phi)\boldsymbol{G}]-\boldsymbol{G}\cdot\nabla(1-\phi) = (1-\phi)\rho\boldsymbol{g}$.

Thus, the above equation eventually becomes

$$\begin{aligned}&\frac{\partial}{\partial t}[(1-\phi)\rho\boldsymbol{V}]+\nabla\cdot[(1-\phi)\rho\boldsymbol{V}\boldsymbol{V}]\\ =\ &(1-\phi)\rho\boldsymbol{g}-(1-\phi)\nabla\boldsymbol{P}_l\\ &+\nabla\cdot(\mu_l\nabla[(1-\phi)\boldsymbol{V}])-\boldsymbol{M}_l^d,\end{aligned}\tag{7}$$

where $\boldsymbol{g}$ is the hypergravity term, $\boldsymbol{g} = N\boldsymbol{g}_0$ and $\boldsymbol{g}_0$ is the acceleration of gravity. $\boldsymbol{M}_l^d$ indicates the dissipative force term due to solidification during melt flow:

$$\begin{aligned}\boldsymbol{M}_l^d &= h\mu_l\phi\frac{\boldsymbol{V}}{W_0}|\nabla\phi|\\ &= \frac{\frac{1}{4}h\mu_l(1+\phi)^2(1-\phi)\boldsymbol{V}}{W_0^2},\end{aligned}\tag{8}$$

where h was determined by plane flow analysis, $h = 2.757$ is a dimensionless constant and the velocity $\boldsymbol{V}$ decays linearly to zero from the liquid phase to the solid phase.

3. Establishment of the numerical model

The data visualization was performed in MATLAB (R2024a). The simulation area is shown in Fig. 2. The shape of the computational domain is rectangular with dimensionless width and height of 240 and 360, respectively, and the meshes are uniform quadrilateral. The number of grid nodes $N_x = 400$, $N_y = 600$ and the distance of meshes $\mathrm{d}x = \mathrm{d}y = 0.6$. The hypergravity directions in this paper are all vertically downwards along the y-axis. Initially, a round grain is placed in the center of the rectangular computational domain, and the supercooled melt flows in from the upper boundary at a uniform vertical flow velocity $\boldsymbol{U}$ with zero horizontal velocity and flows out from the lower boundary. The upper and lower boundaries of the computational domain use forced boundary conditions. The upper boundary is given the melt inflow velocity, the lower boundary is not limited to the melt outflow velocity, and the temperature and pressure of the upper and lower boundaries use constant temperature and constant pressure boundary conditions. The left and right boundaries are characterized by natural boundary conditions, i.e., the gradient of each variable along the boundary normal is zero. The following are the initial conditions:

$$\begin{cases}x^2+y^2<R^2,\ \ \phi=1,\ \ u=0,\ \ \boldsymbol{V}=0,\ \ \boldsymbol{p}=0,\\ x^2+y^2\geq R^2,\ \ \phi=-1,\ \ u=-\Delta,\ \ \boldsymbol{V}=-1,\ \ \boldsymbol{p}=\rho N\boldsymbol{g}_0 y.\end{cases}$$

The initial conditions of the pressure are adopted to be distributed with gradient $N\boldsymbol{g}_0$ gradually increasing along the vertical direction, in order to prevent the numerical calculations caused by the instantaneously applied hypergravity from being difficult to converge. The initial values of the rest of the variables are basically the same as the simulation of free dendritic growth under flow conditions.

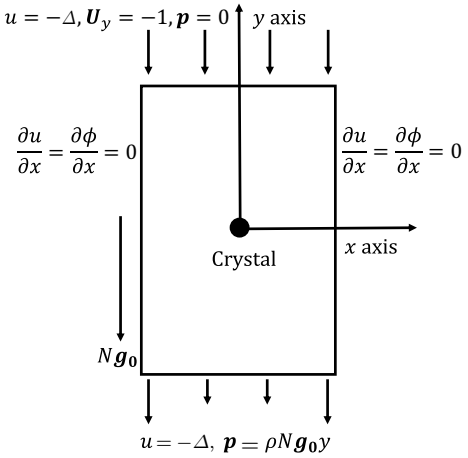


Fig. 2. Schematic diagram of the simulation area and boundary conditions.

In order to save computing time and improve efficiency, this paper is based on symmetry, and only calculates the right half of the computational domain along the y-direction symmetry axis. The diffusion interface thickness W_0 and relaxation time τ_0 are chosen as reference values, and the parameters are dimensionless. The anisotropy coefficient was calculated for two cases: $\varepsilon = 0.03$ and $\varepsilon = 0.05$, corresponding to the anisotropic interfacial energies of copper and nickel, respectively. The computational parameters used in the paper are shown in Table 1.

Table 1. The values and nondimensionalization of all physical quantities.

Physical quantity	Nondimensionalization	Parameter value
Interface thickness W_0		1
Relaxion time τ_0		1
Velocity $\boldsymbol{V}$	$\boldsymbol{V}\left(\frac{\tau_0}{W_0}\right)$	
Pressure term $\frac{\boldsymbol{P}}{\rho}$	$\left(\frac{\boldsymbol{P}}{\rho}\right)\left(\frac{\tau_0}{W_0}\right)^2$	
Gravitational acceleration $\boldsymbol{g}_0$	$\boldsymbol{g}_0\left(\frac{\tau_0^2}{W_0}\right)$	9.81
Heat diffusion coefficient D	$D\left(\frac{\tau_0}{W_0^2}\right)$	4
Kinematic viscosity ν	$\nu\left(\frac{\tau_0}{W_0^2}\right)$	92.4
Initial grain radius R	$\frac{R}{W_0}$	$4.07d_0$
Degree of supercooling Δ		0.55
Coupling parameter λ		6.383
Anisotropy coefficient ε		0.03/0.05
Capillary length d_0		0.139
Density ρ		8.9

4. Results and discussion

4.1. Free dendrite growth under flow

In order to verify the accuracy of the current simulation results, free dendrite growth under flow conditions was first simulated. Subsequently, our results were compared with the Ossen–Ivantsov solution,[26] which is the analytical solution of 2D dendrite growth under flow condition. The analytical solution for 2D dendrite growth under flow condition was given by Bouissou and Pelcé.[27,28] In their theory, the flow is confined to the region of a small Reynolds number. In this premise, Navier–Stokes equations can be reduced to the Ossen flow equations. Based on the tip velocity of dendrite growth $\boldsymbol{V}_t$ and the tip radius of the dendrite R, the number of growing Péclet number $P_{\mathrm{g}} = \boldsymbol{V}_t R/(2D)$ and flow Péclet number $P_{\mathrm{f}} = \boldsymbol{U}R/(2D)$ are defined. Neglecting the interfacial energy and assuming that the shape of the dendrite tip is parabolic, as shown in Fig. 3, they derived the relationships between growth Péclet number (P_{g}), flow Péclet number (P_{f}) and degree of supercooling (Δ),

$$\Delta = P_{\mathrm{g}} \exp\left(P_0\right) I_T\left(\infty\right). \tag{9}$$

Here, $P_0 = P_{\mathrm{g}} + P_{\mathrm{f}}$,

$$\begin{aligned} I_{\mathrm{T}}\left(\infty\right) &= \int_1^{\infty} \exp\left[P_{\mathrm{f}} \int_1^{\xi} \frac{g\left(\zeta\right)}{\sqrt{\zeta}} \mathrm{d}\zeta - P_0 \xi\right] \frac{\mathrm{d}\xi}{\sqrt{\xi}} \\ g\left(\zeta\right) &= \sqrt{\zeta} \frac{\mathrm{erfc}\sqrt{\frac{\zeta Re}{2}}}{\mathrm{erfc}\sqrt{\frac{Re}{2}}} + \left[\exp\left(-\frac{Re}{2}\right)\right. \\ &\quad \left. - \exp\left(-\frac{\zeta Re}{2}\right)\right] \frac{\mathrm{erfc}\sqrt{\frac{2}{\pi Re}}}{\mathrm{erfc}\sqrt{\frac{Re}{2}}}. \end{aligned} \tag{10}$$

Here, Re is the Reynolds number ($Re = \boldsymbol{U}R/\nu$) and ν is the kinematic viscosity.

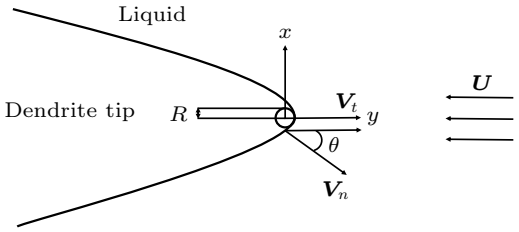


Fig. 3. Schematic diagram of the upstream dendrite arm tip.

Table 2 shows the average growth rates corresponding to the tips of the upstream dendrite arm for different anisotropies and flow velocities, respectively. For $\varepsilon = 0.03$, which is assigned to copper, the growth of dendrites corresponding to the three flow velocities $\boldsymbol{U} = 1$, $\boldsymbol{U} = 2$ and $\boldsymbol{U} = 3.885$ are simulated. For $\varepsilon = 0.05$ which is assigned to nickel, the growth of dendrites corresponding to the two flow velocities $\boldsymbol{U} = 1$ and $\boldsymbol{U} = 2$ are simulated. The results show that for the same anisotropic strength, the higher the flow velocity, the faster the growth rate of the upstream dendrite arm. With the same flow velocities $\boldsymbol{U} = 1$ and $\boldsymbol{U} = 2$, the growth rate of the dendritic upstream tips corresponding to anisotropic strength $\varepsilon = 0.05$ is 22.37% and 21.18% faster than $\varepsilon = 0.03$ respectively. The dendrite growth pattern is consistent with the simulation results of Tong *et al.*[2] and Chen *et al.*[7]

Table 2. The average growth rate of dendrite upstream arm tip under forced convection.

Parameters	ε	0.03	0.03	0.03	0.05	0.05
	$\boldsymbol{U}$	1	2	3.885	1	2
$\boldsymbol{V}_a$		0.9395	1.0193	1.0555	1.1497	1.2352

Table 3. Dendrite tip growth rate and tip radius of the upstream dendrite arms under forced convection, using a quadratic parabola fitted to the tip radius of the dendrite with a fitting width of $10W_0$,[8] calculation parameters: $\Delta = 0.55, \varepsilon = 0.03$ or $\varepsilon = 0.05$, $D = 4$, $Pr = 23.1$.

Parameters	ε	0.03	0.03	0.03	0.05	0.05
	$\boldsymbol{U}$	1	2	3.885	1	2
$\boldsymbol{V}_t$		0.8020	0.9830	0.9200	1.0850	1.0580
R		3.2068	3.4799	4.6804	2.9887	3.1467
P_{g}		0.3215	0.4276	0.5382	0.4053	0.7867
$\boldsymbol{\sigma}$		0.1348	0.0934	0.0552	0.1147	0.1061

Figure 4 shows that when the anisotropy coefficient $\varepsilon = 0.05$ and the dimensionless time $t = 100$, the relationship between the corresponding flow Péclet number P_{f} and growth Péclet number P_{g} for flow velocities is $\boldsymbol{U} = 1$ and $\boldsymbol{U} = 2$. The current simulation results are compared with the simulation results of other scholars and analytical solution. Figure 5 shows the anisotropy coefficient $\varepsilon = 0.03$ and the flow velocities $\boldsymbol{U} = 1$, $\boldsymbol{U} = 2$ and $\boldsymbol{U} = 3.885$, simulation results corresponding to the stabilization of the dendrite tip growth rate, and comparisons are made with the result of Tong *et al.* and the analytical solution. It can be seen from the figures that the current simulation results are more accurate and closer to the analytical solution, indicating the reliability of the current numerical simulation. Table 3 shows an intensive display of the current simulation results.

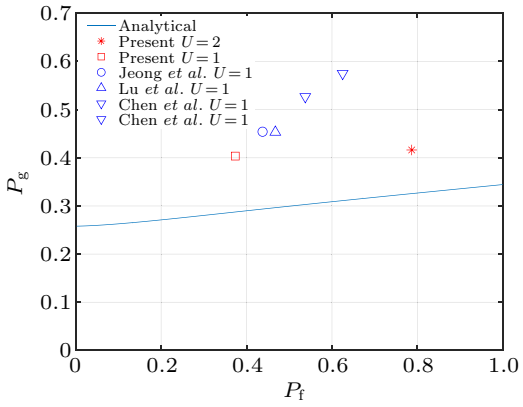


Fig. 4. Anisotropy coefficient $\varepsilon = 0.05$ and the flow velocities $\boldsymbol{U} = 1$ and $\boldsymbol{U} = 2$, the corresponding flow Péclet number P_f and growth Péclet number P_g.

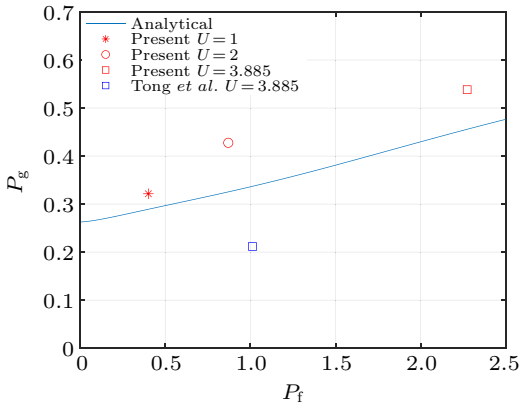


Fig. 5. Anisotropy coefficient $\varepsilon = 0.03$ and the flow velocities $\boldsymbol{U} = 1$, $\boldsymbol{U} = 2$ and $\boldsymbol{U} = 3.885$, the corresponding flow Péclet number P_f and growth Péclet number P_g.

4.2. Free dendritic growth under forced flow with hypergravity

This section investigates the effect of hypergravity on dendrite growth by introducing hypergravity with a flow velocity of $\boldsymbol{U} = 1$ and anisotropy intensity $\varepsilon = 0.03$ as the baseline. Figure 6 shows the dendritic growth morphologies and flow at a dimensionless time of $t = 70$ under different hypergravity conditions. The results indicate that as the hypergravity increases, the flow pattern of the melt will change. Hypergravity reaches $20\boldsymbol{g}_0$, and the small vortices gradually form on the backflow side. The greater the hypergravity, the more pronounced the vortices will become. When hypergravity reaches $35\boldsymbol{g}_0$ under present simulation conditions, the dendritic morphology undergoes significant changes. The upstream arm of the dendrite transitions from upward growth to gradual bifurcation, while the horizontal arms gradually tilt upwards. These phenomena are consistent with the dendrite growth experiment observed under hypergravity.[18,23] As the simulation time increases, the bifurcation regions further develop secondary dendrite branches. In simulations of equiaxed dendritic growth under forced convection in alloys, the deflection of the horizontal dendritic arms and the splitting of the upstream dendritic tip are also clearly observed.[9]

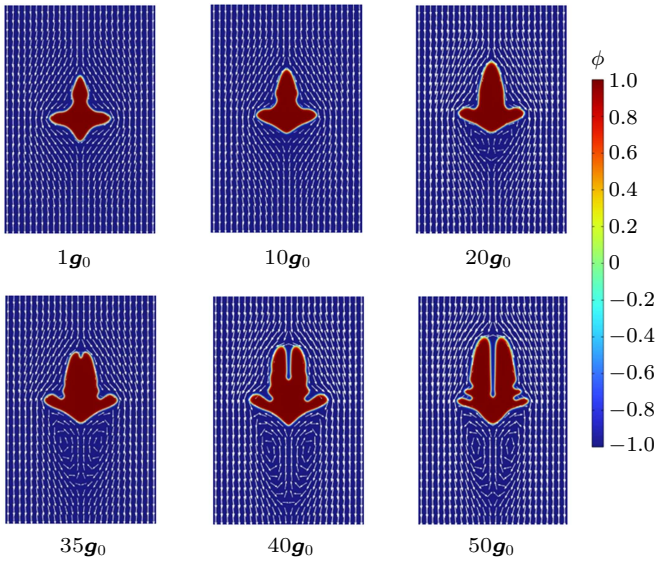


Fig. 6. Dendritic growth morphology and velocity field under different hypergravity conditions at dimensionless time $t = 70$.

Figure 7 shows the dendritic growth phase field, temperature field and velocity field of the simulation region at different time under $50\boldsymbol{g}_0$ hypergravity. In the initial stage, the grain is circular, and under the combined effects of hypergravity and flow, the grain gradually exhibits asymmetric growth. It evolves from circular to a vertically asymmetrical shape, with bifurcation beginning to form at the top when time $t = 10$. At the same time, the horizontal dendritic arms start to tilt upwards. After a period of growth, this asymmetric growth trend becomes more pronounced, and secondary dendrites begin to form on the main dendritic arms, which arise from bifurcation in the upstream dendritic arm at $t = 70$.

Dendritic growth is primarily driven by the temperature gradient, with regions of larger temperature gradient resulting in faster growth rates. By analyzing the temperature gradient and velocity, it can be observed that under vertical flow, the flow speed rapidly decreases at the center of the upstream dendrite tip. This region has difficulty dissipating heat, leading to a smaller temperature gradient. Consequently, there is suppressed dendrite growth. On the other hand, the flow speed on either side of the tip does not slow down, allowing heat to be carried away along the edges of the dendrite, resulting in larger temperature gradients on both sides. As a result, the dendrite grows more quickly in these areas, causing bifurcation. In the backflow growth region, the small vortices gradually form and heat is carried away by vortices, leading to a steep temperature gradient at the dendritic tip, which promotes growth towards the backflow side. This exhibits an inverse trend with downstream dendritic growth under flow.[2,7] For the horizontal dendritic arms, the vortex effect causes a lower temperature gradient on the backflow side, while the temperature gradient on the upstream side is higher due to the flow. This results in the horizontal dendritic arms bending upwards as they grow.

Hypergravity and the flow alter the distribution of the temperature field, creating a significant difference between the temperature fields on the upstream and backflow sides. This trend of temperature field variation causes the horizontal dendritic arms to tilt upwards, the upstream arm to bifurcate and the growth of the downstream dendritic arm is promoted.

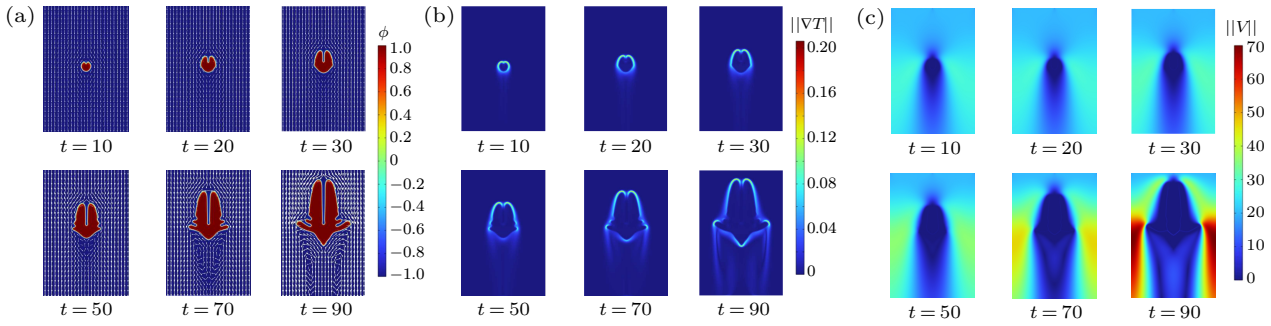


Fig. 7. Dendritic growth under $50\boldsymbol{g}_0$ hypergravity at different times. (a) Phase field and velocity field of the simulation region. (b) Temperature gradient magnitude of the simulation region. (c) Velocity magnitude of the simulation region.

4.3. Effect of hypergravity on dendrite tip interface

The simulation results show that when the hypergravity reaches $35\boldsymbol{g}_0$, as shown in Fig. 6, the dendrite upstream arm will change from upward growth to bifurcation growth. Due to the huge difference in morphology after the bifurcation growth of the dendrite, it is not conducive to quantitatively characterize the effect of hypergravity on the dendrite interface. Therefore, in this paper, only the simulation results before the critical hypergravity of the dendrite morphology transition are considered to analyze the effect of hypergravity on the dendrite tip interface.

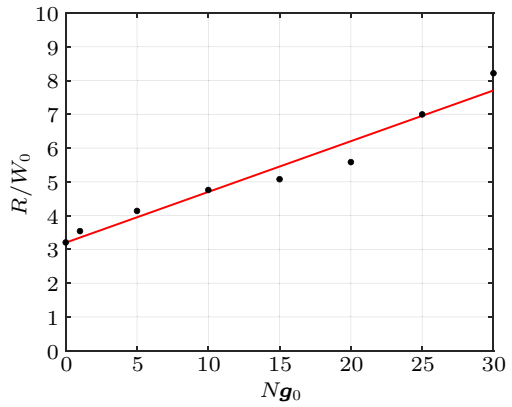


Fig. 8. Variation in the radius at the tip of the upstream dendrite arm (R/W_0) with hypergravity $(N\boldsymbol{g}_0)$ at the dimensionless time $t = 80$.

The experimental results of Abou-Khalil *et al.*[23] showed that at the same cooling rate, the growth rate of dendrite tips accelerate with the increase in hypergravity and the growth rate slows down with the decrease in hypergravity. In this section, we quantitatively examine the upstream dendrite tip growth rate changes with hypergravity and analyze the underlying causes of this phenomenon by the temperature field and flow. Figures 8 and 9 show the variation in the tip radius and the average tip growth rate of the upstream dendrite arm with hypergravity at the moment $t = 80$ respectively. With the increase in hypergravity, the radius of the tip of the upstream dendrite arm exhibits an approximately linear increase, while the average growth rate of the tip is linearly increasing, which fits linearly well. The dendrite tip growth rate trend is consistent with the experimental phenomenon and the simulation of equiaxed dendritic growth in Al–Cu alloy.[22,23] Before the hypergravity reaches $30\boldsymbol{g}_0$, both the average tip growth rate of the upstream dendrite arm and radius of the tip of the upstream dendrite arm exhibit a linear increase with the enhancement of the hypergravity.

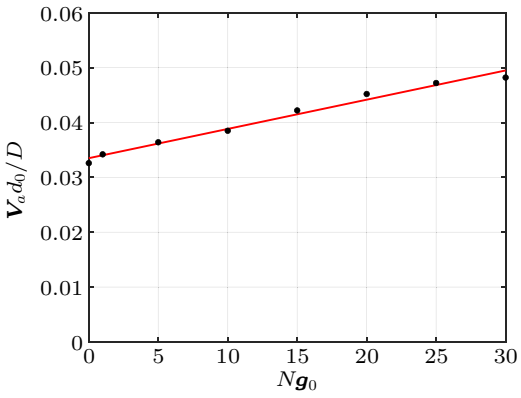


Fig. 9. Variation in the average growth rate at the tip of the upstream dendrite arm $(\boldsymbol{V}_a d_0/D)$ with hypergravity $(N\boldsymbol{g}_0)$ at the dimensionless time $t = 80$.

The causes of these phenomena are mainly hypergravity and flow, which change the temperature field near the dendrite tip interface. Under the effect of hypergravity and flow, the temperature gradient in the vicinity of the dendrite tip of the upstream arm starts to increase, as shown in Fig. 10, and the growth rate of the dendrite tip is accelerated.[6,16,18] With the increase in hypergravity, as shown in Fig. 10, the region of large temperature gradient near the tip of the dendrites begins to gradually flatten from the sharp-type distribution, instead of being concentrated in a smaller area near the tip. The larger temperature gradient begins to spread out on both sides of the tip, which causes the dendrite tip radius to increase and start bifurcating after reaching a critical radius. At the same time,

the tip of the dendritic upstream arm consistently maintains a high temperature gradient. This results in the growth rate of the dendrite tip increasing continuously with the enhancement of hypergravity and will not be affected by this trend of dispersion of the large temperature gradient to the sides of the temperature field. The greater the hypergravity, the more pronounced this tendency becomes and ultimately results in large differences in dendrite morphology.

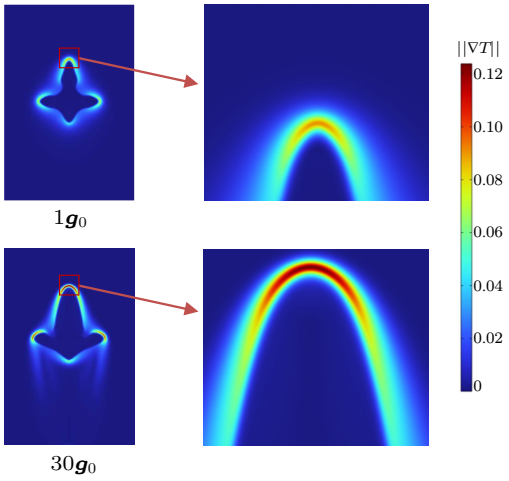


Fig. 10. Temperature gradient magnitude of the upstream dendrite arm under flow and hypergravity at the dimensionless time $t = 80$.

5. Conclusion

Under the hypergravity and melt convection, the temperature field near the dendrite interface will be changed. The greater the hypergravity, the more significant the change in the flow field and temperature field, which leads to large changes in the dendrite morphology. When the hypergravity reaches $35\boldsymbol{g}_0$, the morphology of the dendrite changes significantly. The upstream dendrite arm begins to bifurcate and grows many secondary dendrites, horizontal dendritic arms also grow tilted upwards, and this trend of morphology change becomes more pronounced with increasing hypergravity. The temperature distribution at the tip of the upstream dendritic arm will gradually become smoother from a sharp profile, while backflow will generate vortices with hypergravity increasing. These temperature distribution differences caused by hypergravity and melt convection ultimately lead to significant changes in the dendritic morphology. In addition, the hypergravity and the convection can affect the tip radius and growth rate of the upstream dendrite arm. Before the hypergravity reaches $30\boldsymbol{g}_0$, the greater the hypergravity, the tip radius of the upstream arm tip will gradually increase, while the tip growth rate will be approximately linear.

Future research can be carried out on the following aspect. In practice, due to the difference in solid-liquid phase density, there will be solute buoyancy generated, and the dendrites are moving during the growth process. According to Stokes law, the greater the hypergravity, the faster the rate of dendrite settling, a process that has yet to be investigated using numerical simulation.

Appendix A

The derivation of the hypergravity discontinuous condition at the solid-liquid interface in the momentum equation is based on poromechanics.[29] For the control volume shown in the figure, component 1 represents the solid phase, component 2 represents the liquid phase, Ω_1 represents the solid phase volume, Ω_2 represents the liquid phase volume, Σ represents the interface, $\partial\Omega_1 \cup \Sigma$ represents the solid phase surface, $\partial\Omega_2 \cup \Sigma$ represents the liquid phase surface and $\partial\Omega_t$ represents the outer surface of the entire control volume. A discontinuity exists between the solid and liquid phases, with g representing an arbitrary conserved quantity. $[[g]] = g_2 - g_1$ denotes the discontinuity of the conserved quantity across the interface.

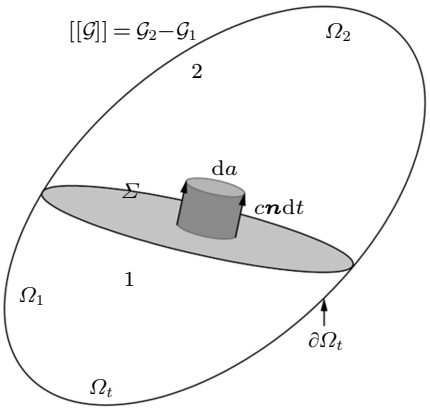


Fig. A1. Schematic diagram of physical quantities (Coussy, 2003).

There is a volume integral over the control volume Ω_t:

$$\frac{\mathrm{d}^{\pi}}{\mathrm{d}t}\int_{\Omega_t} g\,\mathrm{d}\Omega_t = \int_{\Omega_t}\frac{\partial g}{\partial t}\mathrm{d}\Omega_t + \int_{\Omega_t} g\boldsymbol{V}^{\pi}\cdot\boldsymbol{n}\mathrm{d}a. \tag{A1}$$

Coussy volume integral after introducing the interface:

$$\frac{\mathrm{d}^{\pi}}{\mathrm{d}t}\int_{\Omega_\alpha} g\,\mathrm{d}\Omega_t = \int_{\Omega_\alpha}\frac{\partial g}{\partial t}\mathrm{d}\Omega_t + \int_{\partial\Omega_\alpha\cap\partial\Omega_t} g\boldsymbol{V}^{\pi}\cdot\boldsymbol{n}\mathrm{d}a - \int_{\Sigma}[[g]]\,\boldsymbol{c}\cdot\boldsymbol{n}\mathrm{d}a. \tag{A2}$$

Here, Ω_α represents the volume of any phase, where $\alpha = 1$ or 2, $\boldsymbol{c}$ represents the velocity of the interface, $\boldsymbol{n}$ represents the outward unit normal vector of the surface $\partial\Omega_\alpha \cap \partial\Omega_t$, $\boldsymbol{V}^{\pi}$ represents the velocity of the solid or liquid phase, with $\pi = 1$ or 2, and $\mathrm{d}a$ represents an infinitesimal area on the interface.

For $\int_{\Omega_\alpha}\nabla_x\cdot(g\boldsymbol{V}^{\pi})\,\mathrm{d}\Omega_t$, applying the divergence theorem gives the following relationship:

$$\int_{\Omega_\alpha}\nabla_x\cdot(g\boldsymbol{V}^{\pi})\,\mathrm{d}\Omega_t = \int_{\partial\Omega_\alpha\cap\partial\Omega_t} g\boldsymbol{V}^{\pi}\cdot\boldsymbol{n}\mathrm{d}a - \int_{\Sigma}[[g]]\,\boldsymbol{V}^{\pi}\cdot\boldsymbol{n}\mathrm{d}a. \tag{A3}$$

Based on geometric relationships, $\Omega_t = \Omega_1 \cup \Omega_2$, and $\partial\Omega_t = (\partial\Omega_1 \cap \partial\Omega_t) \cup (\partial\Omega_2 \cap \partial\Omega_t)$. In the solid or liquid phase, substituting Eq. (3) into Eq. (2) gives

$$\frac{\mathrm{d}^{\pi}}{\mathrm{d}t}\int_{\Omega_\alpha} g\,\mathrm{d}\Omega_t = \int_{\Omega_\alpha}\left(\frac{\partial g}{\partial t} + \nabla_x\cdot\left(g\boldsymbol{V}^{\pi}\right)\right)\mathrm{d}\Omega_t + \int_{\Sigma}\left[\left[g\left(\boldsymbol{V}^{\pi}-\boldsymbol{c}\right)\right]\right]\cdot\boldsymbol{n}\,\mathrm{d}a. \tag{A4}$$

Substitute the conserved quantity $g = \rho\boldsymbol{V}$, and use the integral form of the momentum equation:

$$\frac{\mathrm{d}}{\mathrm{d}t}\int_{\Omega_\alpha}\rho\boldsymbol{V}\,\mathrm{d}\Omega_t = \oint_{\partial\Omega_\alpha}\boldsymbol{T}\cdot\boldsymbol{n}\,\mathrm{d}a + \int_{\Omega_\alpha}\rho\boldsymbol{b}\,\mathrm{d}\Omega_t. \tag{A5}$$

Here, ρ is the density, $\boldsymbol{V}$ is the flow velocity, $\boldsymbol{T}$ is the shear stress and $\boldsymbol{b}$ is the gravitational acceleration. Substituting Eq. (5) into Eq. (4), in the liquid phase with volumeΩ_2, we have

$$\begin{aligned}&\int_{\Omega_2}\left(\frac{\partial\left(\rho\boldsymbol{V}\right)}{\partial t} + \nabla_x\cdot\left(\rho\boldsymbol{V}\boldsymbol{V}\right)\right)\mathrm{d}\Omega_t \\ &-\int_{\Sigma}\left[\left[\rho\boldsymbol{V}\left(\boldsymbol{V}-\boldsymbol{c}\right)\right]\right]\cdot\boldsymbol{n}\,\mathrm{d}a \\ =&\int_{\partial\Omega_2\cap\partial\Omega_t}\boldsymbol{T}\cdot\boldsymbol{n}\,\mathrm{d}a + \int_{\Sigma}\left[\left[\boldsymbol{T}\right]\right]\cdot\left(-\boldsymbol{n}\right)\mathrm{d}a + \int_{\Omega_2}\rho\boldsymbol{b}\,\mathrm{d}\Omega_t.\end{aligned} \tag{A6}$$

Note that in the momentum equation, the direction of $\boldsymbol{V}$ is taken as the positive direction. When substituting $[[g(\boldsymbol{V}^{\pi}-\boldsymbol{c})]] = [[\rho\boldsymbol{V}(\boldsymbol{V}-\boldsymbol{c})]]$, the direction of $\boldsymbol{c}$ remains unchanged, meaning the direction of the velocity is aligned with the normal to the interface. The direction of the interface is opposite to the normal of $\partial\Omega_2 \cap \partial\Omega_t$. Therefore, when substituting $\boldsymbol{g} = \rho\boldsymbol{V}$ into Eq. (4), $\boldsymbol{n}$ should be replaced with $-\boldsymbol{n}$ to maintain consistency in the directions of the vectors. Simplifying, we obtain

$$\begin{aligned}&\int_{\Omega_2}\left(\frac{\partial\left(\rho\boldsymbol{V}\right)}{\partial t} + \nabla_x\cdot\left(\rho\boldsymbol{V}\boldsymbol{V}\right)\right)\mathrm{d}\Omega_t \\ &-\int_{\Sigma}\left[\left[\rho\boldsymbol{V}\left(\boldsymbol{V}-\boldsymbol{c}\right)-\boldsymbol{T}\right]\right]\cdot\boldsymbol{n}\,\mathrm{d}a \\ =&\int_{\partial\Omega_2\cap\partial\Omega_t}\boldsymbol{T}\cdot\boldsymbol{n}\,\mathrm{d}a + \int_{\Omega_2}\rho\boldsymbol{b}\,\mathrm{d}\Omega_t.\end{aligned} \tag{A7}$$

For $\int_{\Omega_2}\rho\boldsymbol{b}\,\mathrm{d}\Omega_t$, a treatment similar to that for the shear stress is applied. The volume integral of the body force over the control volume is transformed into a surface integral over the control volume surface. By applying the Gauss divergence theorem, we obtain

$$\int_{\Omega_2}\rho\boldsymbol{b}\,\mathrm{d}\Omega_t = \int_{\Omega_2}\mathrm{div}\left(\boldsymbol{G}\right)\mathrm{d}\Omega_t = \oint_{\partial\Omega_2}\boldsymbol{G}\cdot\boldsymbol{n}\,\mathrm{d}\partial\Omega_t. \tag{A8}$$

Here, $\boldsymbol{G} = (G_x, G_y, G_z) = (\int\rho b_x\,\mathrm{d}x, \int\rho b_y\,\mathrm{d}y, \int\rho b_z\,\mathrm{d}z)$, where b_x, b_y and b_z are the components of the gravitational acceleration in the three directions. The remaining steps follow the same treatment as for the shear stress:

$$\begin{aligned}&\int_{\Omega_2}\left(\frac{\partial\left(\rho\boldsymbol{V}\right)}{\partial t} + \nabla_x\cdot\left(\rho\boldsymbol{V}\boldsymbol{V}\right)\right)\mathrm{d}\Omega_t \\ &-\int_{\Sigma}\left[\left[\rho\boldsymbol{V}\left(\boldsymbol{V}-\boldsymbol{c}\right)-\boldsymbol{T}\right]\right]\cdot\boldsymbol{n}\,\mathrm{d}a \\ =&\int_{\partial\Omega_2\cap\partial\Omega_t}\boldsymbol{G}\cdot\boldsymbol{n}\,\mathrm{d}a + \int_{\Sigma}\left[\left[\boldsymbol{G}\right]\right]\cdot\left(-\boldsymbol{n}\right)\mathrm{d}a \\ &+\int_{\partial\Omega_2\cap\partial\Omega_t}\boldsymbol{T}\cdot\boldsymbol{n}\,\mathrm{d}a.\end{aligned} \tag{A9}$$

Simplifying, we obtain

$$\begin{aligned}&\int_{\Omega_2}\left(\frac{\partial\left(\rho\boldsymbol{V}\right)}{\partial t} + \nabla_x\cdot\left(\rho\boldsymbol{V}\boldsymbol{V}\right)\right)\mathrm{d}\Omega_t \\ =&\int_{\partial\Omega_2\cap\partial\Omega_t}\boldsymbol{G}\cdot\boldsymbol{n}\,\mathrm{d}a + \int_{\partial\Omega_2\cap\partial\Omega_t}\boldsymbol{T}\cdot\boldsymbol{n}\,\mathrm{d}a \\ &+\int_{\Sigma}\left[\left[\rho\boldsymbol{V}\left(\boldsymbol{V}-\boldsymbol{c}\right)-\boldsymbol{T}-\boldsymbol{G}\right]\right]\cdot\boldsymbol{n}\,\mathrm{d}a.\end{aligned} \tag{A10}$$

The above equation is the general form of the momentum equation with an interface, after introducing body force into the momentum equation. Since the solid and liquid phases are assumed to have equal density and the fluid is incompressible, ρ is a constant. Therefore, the integral of the body force can be calculated by simply finding an antiderivative of the integrand

$$\boldsymbol{G} = \left(\int\rho b_x\,\mathrm{d}x, \int\rho b_y\,\mathrm{d}y, \int\rho b_z\,\mathrm{d}z\right) = \left(x\rho b_x, y\rho b_y, z\rho b_z\right). \tag{A11}$$

Acknowledgement

This work was supported by the National Natural Science Foundation of China (Grant No. 52588202). The authors would like to thank Dr. Wei-Long Ren from the Institute of Hypergravity Science and Technology at Zhejiang University for his valuable assistance in the use of the computing cluster.

References

[1] Beckermann C, Diepers H J, Steinbach I, Karma A and Tong X 1999 *J. Comput. Phys.* **154** 468
[2] Tong X, Beckermann C, Karma A and Li Q 2001 *Phys. Rev. E* **63** 061601
[3] Zhang Z D, Cao Y T, Sun D K, Xing H, Wang J C and Ni Z H 2020 *Chin. Phys. B* **29** 028103
[4] Zhu C S, Gao Z H, Lei P, Feng L and Zhao B R 2022 *Chin. Phys. B* **31** 068102
[5] Lu Y L 2003 *Phase-field modeling of three-dimensional dendritic solidification coupled with fluid* flow (Ph.D. dissertation) (Iowa City: The University of Iowa)
[6] Jeong J H 2001 *Phys. Rev. E* **64** 041602
[7] Chen C C, Tsai Y L and Lan C W 2009 *Int. J. Heat Mass Transfer* **52** 1158
[8] Gong T Z, Chen Y, L D Z, Cao Y F and Fu P X 2019 *Int. J. Heat Mass Transfer* **135** 262
[9] Qiu Y Q, Wu M W, Qin X P and Xiong S M 2024 *Chin. Foundry* **21** 125
[10] Wang J, Li X K, Liu C and Shi Y 2016 *Chin. J. Solid Mech.* **37** 1 (in Chinese)
[11] Hua C W, Gan Z H, Jiang P H, Sun Y and Lu Z H 2018 *Spec. Cast. Nonferrous Alloys* **38** 327 (in Chinese)

[12] Xiong M, Gan Z H, Liang Y, Feng J J, Lu Z H and Liu J 2017 *J. Mater. Sci. Eng.* **35** 1005 (in Chinese)
[13] Scotti K L, Northard E E, Plunk A, Tappan, B C and Dunand D C 2017 *Acta Mater.* **124** 608
[14] Zhang N, Luo X, Feng S and Ren Y 2014 *Mater. Sci. Technol* **30** 499
[15] Wu H, Wu C, Lu Y, Jiang P, Gan Z and Liu J 2020 *Adv. Eng. Mater.* **22** 2000360
[16] Li Z Y, Chen C L and Duan M M 2007 *Spec. Cast. Nonferrous Alloys* **27** 753 (in Chinese)
[17] Jin Q W, Chen C L, Duan M M and Li Z Y 2007 *J. Inorg. Mater.* **22** 1015 (in Chinese)
[18] Zimmermann G, Hamacher M and Sturz L 2019 *J. Cryst. Growth* **512** 47
[19] Zhang Z H, Hou X, Zhang Y, Wei H and Wang J 2022 *Acta Mech. Sin.* **38** 122031
[20] Steinbach I 2009 *Acta Mater.* **57** 2640
[21] Viardin A, Zollinger J, Sturz L, Apel M, Eiken J, Berger R and Hecht U 2020 *Comput. Mater. Sci* **172** 109358
[22] Zhang Y Y, Do R F, Wan J S, Liu X L and Wen Z 2024 *Heliyo* **10** e27008
[23] Abou-Khalil L, Salloum-Abou-Jaoude G, Reinhart G, Pickmann C, Zimmermann G and Nguyen-Thi H 2016 *Acta Mater.* **110** 44
[24] Karma A and Rappel W J 1996 *Phys. Rev. E* **53** R3017(R)
[25] Karma A and Rappel W J 1998 *Phys. Rev. E* **57** 4323
[26] Ivantsov G P 1947 *Dokl. Akad. Nauk SSSR* **58** 567
[27] Alexandrov D V and Galenko P K 2014 *Phys. Usp.* **57** 771
[28] Alexandrov D V and Galenko P K 2020 *Philos. Trans. R. Soc. A* **379** 0325
[29] Coussy O 2004 *Poromechanics* (John Wiley & Sons, Chichester, UK) pp. 14–15